

Quantification of the pore structures of Malan loess and the effects on loess permeability and environmental significance, Shaanxi Province, China: an experimental study

Xi'an Li¹ · Lincui Li¹

Received: 14 March 2017 / Accepted: 21 July 2017 / Published online: 1 August 2017
© Springer-Verlag GmbH Germany 2017

Abstract The pore microstructures of loess control the porosity and permeability of the loess, affecting the patterns of groundwater flow and the transport of contaminants. In the present study, the pore microstructure of Malan loess was investigated quantitatively in samples from five different loess layers. Specimens were examined via SEM, and pore microstructure parameters were determined using the digital image analysis method. Pore structures (including pore area ratio (PAR), pore size distribution, pore shape and pore morphology), the effects of the pore structure on loess permeability and the environmental significance of these factors are discussed in this paper. The results indicate that the samples of five loess layers in this study are considered to be porous soil, according to both the PAR and porosity values. The number of micropores, small pores, mesopores and macropores decreased significantly. The differences in number were mainly due to the significant reduction in the number of round pores, indicating that round pores tend to be small. In terms of area, micropores, small pores, mesopores and macropores were dominated by elongated and irregular pores. The macro- and mesopore structural characteristics of loess determined the transfer characteristics of groundwater and pollutants in the loess. Additionally, the 62% area reduction in the area of elongated or irregular macro- and mesopores and the decreasing

connectivity from top to bottom layers caused by the deformation and destruction of the pores due to the overlying soil reduced the permeability and the water/pollutant migration rate with depth.

Keywords Malan loess · Microstructure · Pore shape · Pore morphology · Environmental significance

Introduction

Loess is widely distributed around the world and is common in China. Loess covers almost 7% of the total land territory of China. Recently, large-scale engineering projects have been implemented in the loess area of northwest China (Li et al. 2014a), resulting in large changes in the natural loess structure and consequential effects on the flow of water and the transport of contaminants within the loess. To promote the establishment of ecological civilization in the Loess Plateau of China, various studies related to hydrodynamics and water pollution in loess areas have been performed (Li et al. 2014b, c, d, e, 2016a, b, c, d; Wu and Sun 2016). The flow of water and the transport of contaminants in loess are controlled by the porosity, which is regulated by the structure of the loess. However, research on this aspect is rare.

Soil and loess are homogeneous, porous, friable, and non-stratified media. The microstructure is one of the most important parameters affecting material behavior. For natural unsaturated loess, the microstructure affects water retention properties (Muñoz-Castelblanco et al. 2012), water permeability (Romero et al. 1999; Romero and Simms 2008) and montmorillonite layer aggregation. Pore shape, especially elongated transmission pores, is essential for root growth, water movement, water storage, and air

This article is a part of a Topical Collection in Environmental Earth Sciences on Water resources development and protection in loess areas of the world, edited by Drs. Peiyue Li and Hui Qian.

✉ Lincui Li
llc934157098@163.com; 934157098@qq.com

¹ College of Geology Engineering and Geomatics, Chang'an University, Xi'an, Shaan xi 710064, China

exchange in porous media (Vandenbygaert et al. 1999; Pagliai et al. 2004). In soils, pore orientation is related to its consolidation (Cetin 2004). The shear strength reduction in loess results from structural changes (Wen and Yan 2014); additionally, collapse processes can lead to smaller pore sizes and more oriented pore distributions, which result in a decrease in shear strength. For cement-based materials, the pore structure plays a crucial role in the mechanical properties, transport properties, and durability (Promentilla et al. 2009; Wan and Xu 2014). For clay, changes in the pore microstructure are closely connected to its hydration mechanisms (Rasa et al. 2012). To study aging effects in compacted bentonite, Delage et al. (2006) investigated inter-aggregate porosity and the very thin porosity not intruded by mercury. Delage (2010) also examined the intact and remolded microstructure, to better understand the relationship between microstructure and sensitivity. An interesting correlation between the compressibility coefficient and the slope of the cumulative pore size distribution curve is observed in Champlain clays. Mitchell indicated that the changes in fabric orientation led to engineering property differences.

In addition, natural or artificial causes and changes in the environment can lead to the internal structure of a soil (Li et al. 2014a, 2017; Pires et al. 2008). For example, soil shrinkage due to drying can generate planar voids, and ice lenses that formed during soil freezing can generate elongated voids and platy or lenticular structures (VandenBygaert et al. 1999). Winter freezing causes a platy pedality created by the growth of ice segregation blades, and desiccation causes a prismatic pedality in silt loam soils (Sveistrup et al. 2005). Seasonal swelling and shrinking contribute to large structural changes in clay soils (Messing and Jarvis 1990). For example, Bottinelli et al. (2016) proposed that soil shrinkage increased the volume of pores as well as their connectivity. Round pores or channels in loess are generated from root growth, burrowing animal activity, structural collapses, and changes in inter-aggregate pore spaces due to shrinkage pressure (Rasa et al. 2009).

There are numerous experimental techniques to characterize material structure, such as mercury intrusion porosimetry (MIP), optical microscopy, gas adsorption, X-ray and CT. Pore structure changes in cement pastes during wetting and drying cycles were characterized by Aono et al. (2007) using water vapor adsorption and mercury intrusion porosimetry. Bernardes et al. (2015) analyzed the pores of a Portland cement composite. Gutierrez et al. (2009) investigated the deformation and microstructure of clayey soils induced by collapse using an optical microscope. To determine pore characteristics quantitatively, Munkholm et al. (2012) quantified pore structures in undisturbed field moist soil assessed from X-ray and CT. Levitz (2007) and Yang et al. (2014) further investigated

volume porosity, pore size distribution and connectivity via 3D imaging of porous media. Scanning electron microscopy (SEM) has been widely used to study the micropore structure of porous material. Delage (2010) and Romero and Simms (2008) described the microstructure changes in sensitive clay during compression and the microstructure of partially saturated soils, respectively, based on MIP and SEM. These works showed that the measured K_{fs} values were strongly correlated with the total inter-aggregate (macro-) porosity, estimated from a simple model of soil shrinkage (Messing and Jarvis 1990). Much valuable research has been conducted to characterize other porous media structures using SEM. For example, Nie et al. (2015) analyzed the pore structure of coals based on gas adsorption and SEM. Additionally, the pore microstructures of the catalyst layer were evaluated by Klaver et al. (2015), who found that the circularity of shale pores exhibits a left-skewed distribution, a main pore convexity of 1 and a left-skewed elongation distribution.

Little research appears to have focused on the influence of depth on pore structure. In this paper, five samples from different depths were analyzed quantitatively using SEM and Image-Pro Plus 6.0 (IPP). The pore structure, including pore area ratio (PAR), pore size distribution, pore shape, and pore morphology, was characterized. The aim was to study the effect of depth on the loess microstructure. The environmental significance of loess microstructure is also discussed in this paper.

Experimental

The basic soil mechanics test

As the top layer of a Pleistocene loess–paleosol sequence, the Malan loess is widely distributed across the Loess Plateau in China (Fig. 1) with a thickness up to 30 m. Thus, the Malan loess acts as the main substrate for industrial production, daily life, and construction activities. In this study, the microstructures of the Malan loess were taken as the research focus.

Natural Malan loess samples were collected from Yan'an City, situated on the Loess Plateau of China (Fig. 1). The sample depths were 2, 4, 6, 8 and 10 m. The basic physical properties of Malan loess in the five loess samples are presented in Table 1. Natural Malan loess samples have a low water content that varies between 7.8 and 15.5%, as measured using the oven-drying method. The liquid and plastic limits of the five loess samples were tested using liquid–plastic combined tests and ranged from 29.3 to 30.6% and from 15.9 to 17.5%, respectively; thus, the sampled material can be regarded as plastic loess. A laser particle sizer was applied to test the grain size content

Fig. 1 Distribution of Malan loess on the Loess Plateau (Q_4^{eol} represents Holocene alluvial sand. Q_4^{al+pl} represents Quaternary lacustrine clay and sandy gravel. Q_4^{fgl+pl} represents Quaternary glacial and gravel deposits. Q_4^{al+pl} represents Holocene alluvial and diluvial loess soil. Q_3^{eol} means the Late Pleistocene eolian loess. AnN_2 means pre-Pliocene bedrock.)

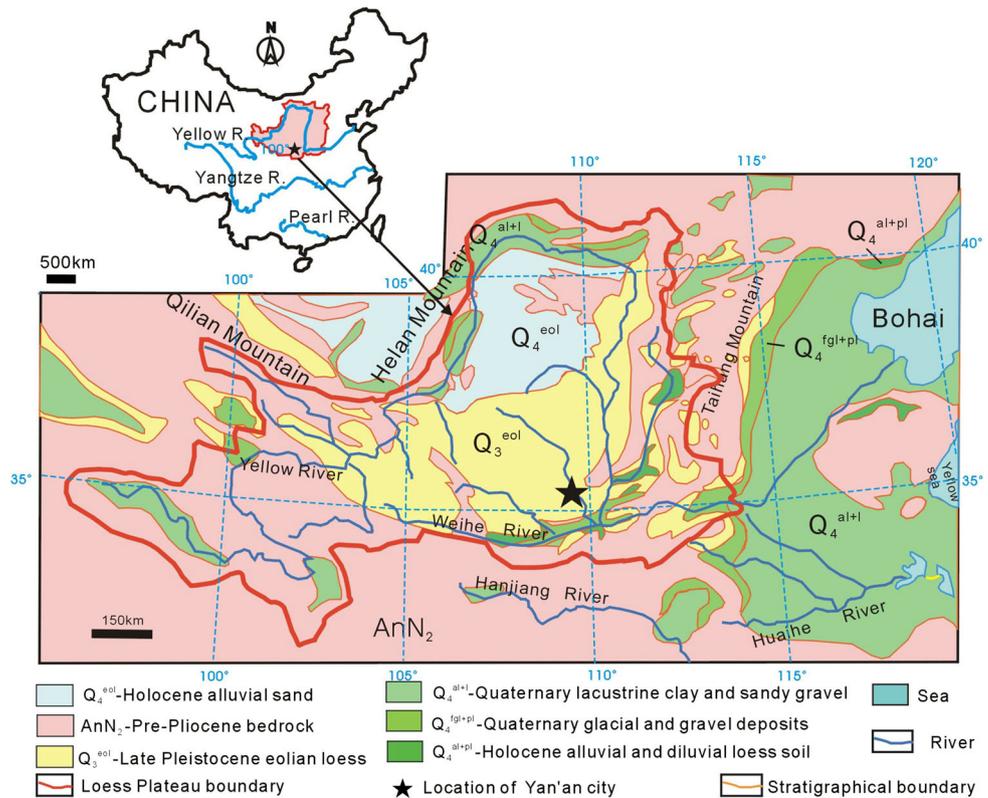


Table 1 The basic properties of the loess

Properties	Value				
Depth (m)	2	4	6	8	10
Water content (%)	11.9	14.1	15.5	7.8	8.9
Liquid limit (%)	30.6	29.3	30.1	29.9	30.1
Plastic limit (%)	17.5	16.0	16.4	15.9	16.3
Unit weight (kN/m ³)	16.2	16.4	16.4	15.4	15.7
Porosity (%)	44.0	39.5	40.5	39.2	42.1
Sand (%)	11.29	15.75	17.12	17.13	19.86
Silt (%)	65.60	62.24	59.75	60.37	62.64
Clay (%)	23.11	22.03	23.13	22.50	17.50

of the loess. The sand content in the loess samples ranged from 11.29 to 19.86%, the silt content ranged from 59.75 to 65.60%, and the clay content ranged from 17.5 to 23.13%. Thus, the sampled material represents a type of fine-grained loess. A ring sampler was applied to test unit weight. The void ratios ranged from 39.5 to 43.2%; thus, the sampled material represents loose or porous loess with high compressibility.

Specimen preparation and test procedures

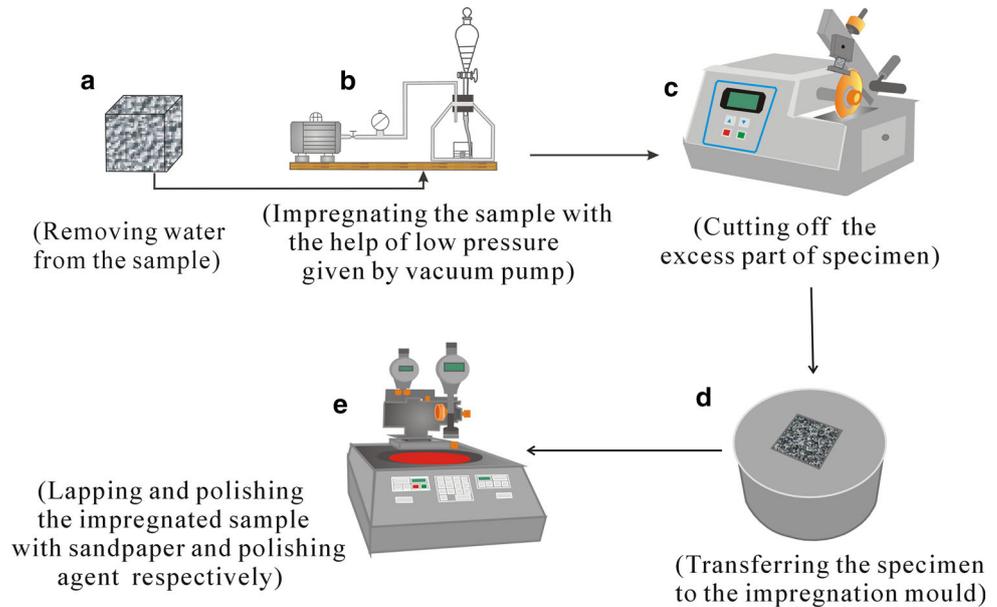
Figure 2 shows the process of specimen preparation and test procedures. (1) The cuboid samples were cut from

natural features and dehydrated under laboratory conditions. Long dehydration durations and stable laboratory temperature and humidity conditions allow for minimal dimensional changes and negligible effects on soil structure (Fig. 2a). (2) To facilitate the intrusion of resin throughout the loess pores, the pore-filling process was assisted by minutes-long vacuum treatments using a vacuum pump (Fig. 2b). Samples were impregnated with resin until no more air bubbles appeared and sealed for thirty days to allow the resin to harden, followed by drying in an oven for three days at 60 °C.

Prior to mixing with acetone (solvent), the epoxy resin (cement) was treated with a water bath to dilute it. Then, the epoxy resin was dissolved in acetone and stirred constantly until a clear solution was obtained. Ethylenediamine (hardener) and dibutyl phthalate (plasticizer) were added in order. Epoxy resin, acetone, ethylenediamine and dibutyl phthalate were mixed thoroughly at a 60:30:4:1 volume ratio.

(3) Specimens impregnated with hardened resin were cut with specific machines to eliminate the excess parts (Fig. 2c). (4) To protect the specimen from disturbance or breakage during later polishing, specimen was transferred into a cylindrical mold full of cold mounting material and then left to become embedded over the course of many days (Fig. 2d). (5) The MultiPrep™ system, which performs an automatic grinding process, was applied for rough grinding and polishing via silicon carbide paper and a

Fig. 2 The procedures of sample preparation



polishing agent, respectively (Fig. 2e). The preparation of loess microstructure specimens was deemed complete when the surface of the samples became shiny and the structure of the loess could be observed clearly under an optical microscope.

Image post-processing

Polished samples were scanned at a magnification of $800\times$ using SEM (Quanta FEG, 10 kV, the working distance is 11.4 mm). Four images of each specimen were collected and were spliced together to increase the analysis area, which can greatly enhance accuracy of the quantitative analysis. Image post-processing and data acquisition were conducted using IPP. First, the brightness and contrast of the raw images were enhanced to make the boundaries of the pores and particles easier to recognize (Fig. 3a). Then, a median filter was applied to modify the isolated erroneous pixels and remove random and high impulse noise (Fig. 3b). A low-pass filter was then applied to eliminate random noise, making image segmentation easier and more accurate (Fig. 3c). Finally, pore boundaries were identified automatically based on the HSI color model (Fig. 3d). After delineating and locating the boundaries between loess particles and pore spaces successfully, the images were binarized (Fig. 3e). The particles and pores were masked with white and black, respectively, enabling the quantification and visualization of the pore microstructure (Fig. 3f).

Pore microstructure parameter acquisition

Raw images, binary images and PAR values for the five loess samples are presented in Fig. 4. Image analysis

allows for quantification of the microstructure of each available pore, including pore area (A_{pore}), total pore area ($A_{\text{total pore}}$), the area of the image (A_{total}), pore mean diameter (D_{pore}), pore perimeter (P_{pore}), pore long and short axis lengths (L_{pore} , W_{pore}), and area of the convex hull of the pore ($A_{\text{convex hull}}$). Pores surrounding the loess clods and particles became progressively disconnected as the depth increased (Fig. 4), which is similar to the findings of Fener and Yesiller (2013). The number, size, and connectivity of pores decreased as well, which can be communicated qualitatively via the black space occupied by pores in the images.

Results and discussion

Pore area ratio (PAR) and porosity

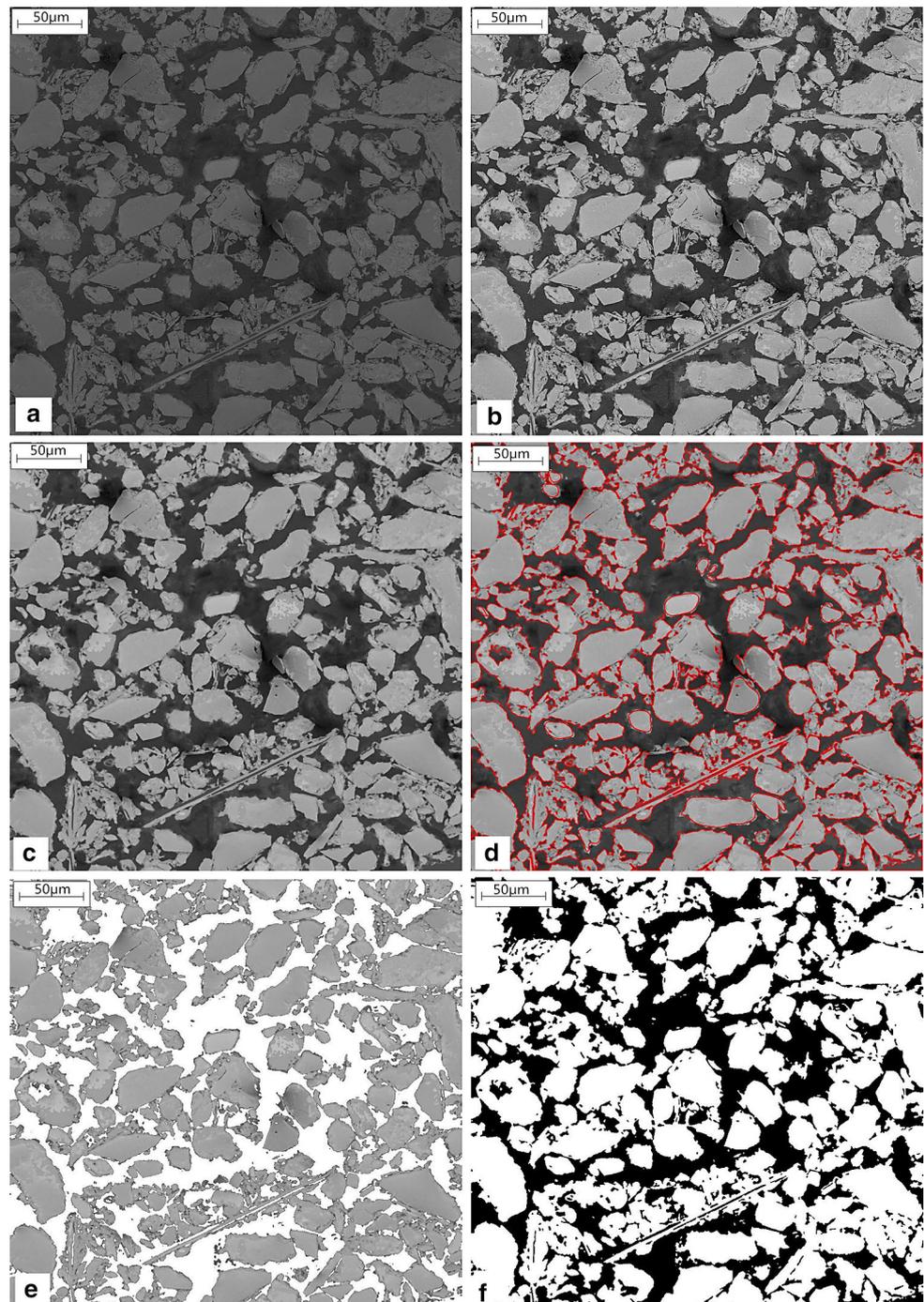
The pore area ratio (PAR), calculated directly from the binary images, was introduced to quantify the pore area in the microscopic images.

$$\text{PAR} = \frac{A_{\text{total pore}}}{A_{\text{total}}} \times 100\% \quad (1)$$

where $A_{\text{total pore}}$ is the total pore area and A_{total} is the area of the SEM image.

The PAR values of the samples of five loess layers are presented in Fig. 5 using the pie charts in the top right corners of the slides in Fig. 4. Based on image analysis, soil can be classified as dense when its porosity is $<10\%$, moderately porous when its porosity is between 10 and 25%, and porous when its porosity is between 25 and 40%. Therefore, the five samples at different depths were

Fig. 3 Image post-processing



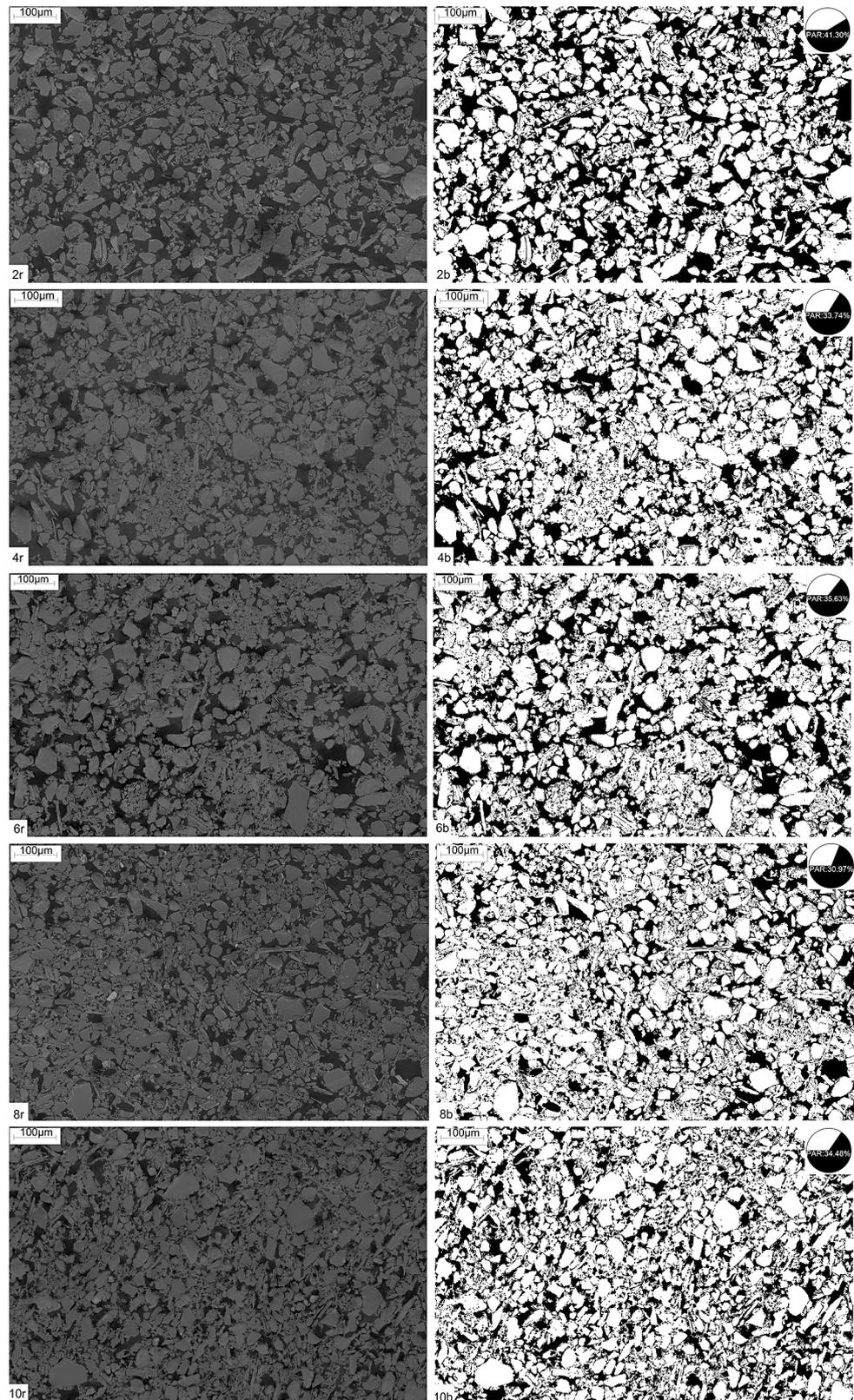
considered porous, because their PARs were all >30%, which is consistent with the classification of the loess based on porosity (Table 1). The general trend of the PAR values obtained from image analysis was validated by comparing it with the porosity obtained from phase relationships (Fig. 5). The change in PAR was in good agreement with the variation in the porosity of each loess layer, thereby supporting the assumption that pores obtained from

segmented SEM images were representative of the pore distribution in the loess.

Pore size distribution

The pore size and area percentage distribution of the five loess samples are presented in Fig. 6. The artificial defect in post-processing and image noise cannot be avoided

Fig. 4 SEM raw images and binary images of the five samples (The designation code on the *bottom left* was designed to differentiate the images. The first number indicates depth; “r” and “b” indicate the raw image and binary image, respectively. The pore area ratios are shown with pie charts at the *top right* corners.)



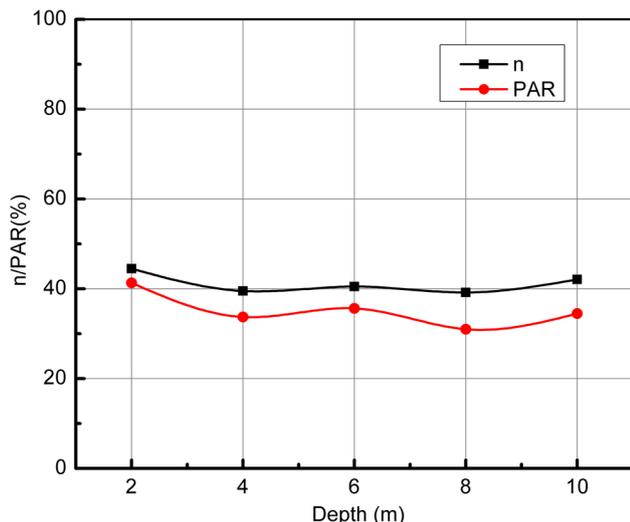


Fig. 5 Comparison between the pore area ratio and porosity

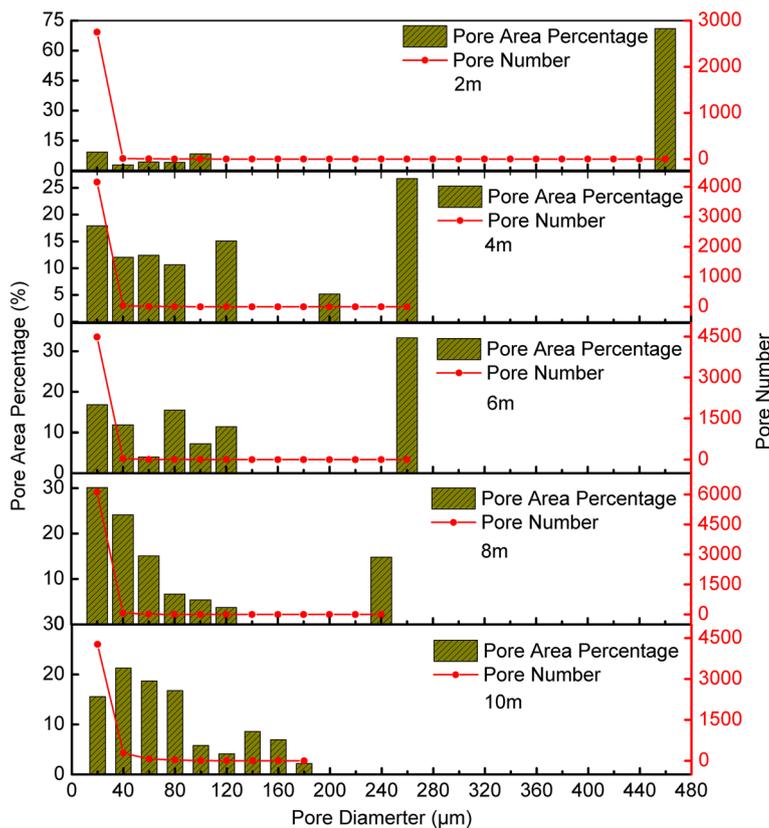
completely, and pores smaller than 1 μm constitute only 1–2.7% of the total pore area. Thus, only pores larger than 1 μm, which comprise the majority of the loess structure, were considered in this paper.

For all specimens, the range of pore diameter was 1–460 μm as determined via digital analyses. Approximately more than 95% of the pores had a diameter between

1 and 20 μm for specimens from each loess layer. The number of pores decreased with increasing pore diameter. When the diameter was larger than 40 μm, the number of pores became stable.

However, there were differences between each of the samples. It can be seen from the maximum value of each horizontal axis that the diameter of the largest pore decreased with depth. Additionally, the pore size distribution of some specimens did not contain medium-sized pores (pore diameters ranged between 120 and 440 μm for the specimen from 2 m, 100 and 240 μm for the specimen from 4 m, 140 and 240 μm for the specimen from 6 m, 140 and 220 μm for the specimen from 10 m). Medium-sized pores are connected to larger pores in the top layer, facilitating a good connectivity between macropores in top layer. This pattern explains why the area percentage of pores in mid-range diameters seems to be lower or even lacking in Fig. 6. Moreover, the area percentage of pores larger than 200 μm in each specimen decreased with depth (Fig. 6), medium-sized pores start to gradually appear, the area percentage of pores smaller than 120 μm increased. The pressure of the overlying loess is inferred to lead to the deformation and breakage of larger pores, squeezing them into smaller pores. This trend was even more pronounced at 10 m. This result is basically consistent with the literature (Fener and Yesiller 2013). Thus, greater overburden

Fig. 6 Pore size distribution (Pores in loess are classified into intervals of 20 μm. The pore area percentage in each interval is presented by a histogram, and the variation in the number of pore in each interval is illustrated by the red line.)



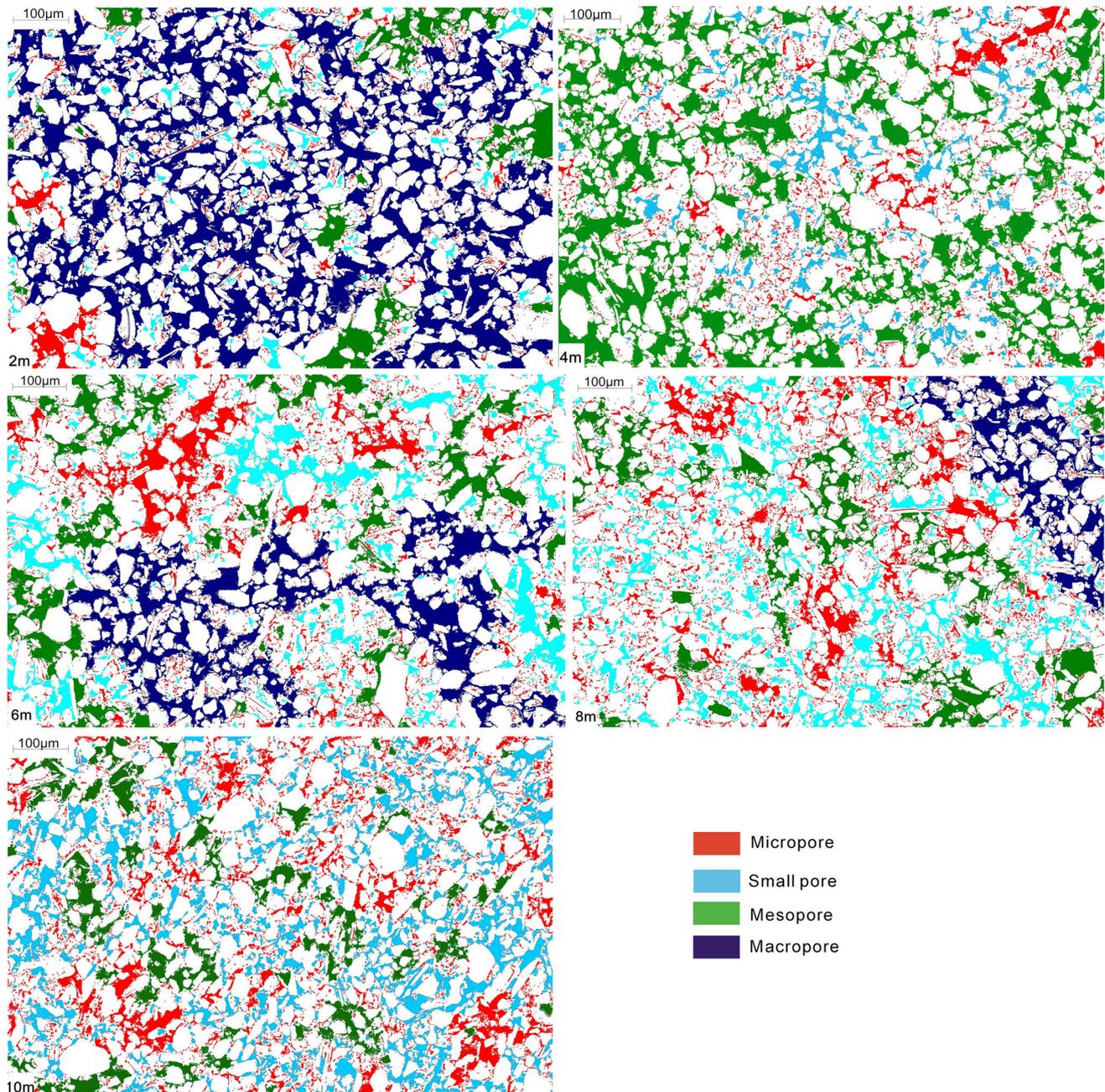


Fig. 7 Pore distribution of specimens at the different depths

pressure reduces the size of large pores, and the physical and engineering properties of loess at depth will differ from those of loess in the top layer.

The area and number distribution of different types of pores

Pores in loess can be classified into four types based on the mean radius, with micropores having a mean radius from 0

to 1 μm , small pores from 1 to 4 μm , mesopores from 4 to 16 μm , and macropores larger than 16 μm .

Figure 7 provides an insight into the change in area and connectivity of different pore types. For the sample from a depth of 2 m, smaller pores are connected to larger pores, facilitating good connectivity between macropores, which is consistent with the conclusion drawn from Fig. 6. However, the connectivity becomes weaker as the burial depth gradually increases. Simultaneously, the area of the

Table 2 Number and area percentage of four types of pores

Depth (m)		2	4	6	8	10
Pore number	Micropore	94.45	93.93	93.95	92.19	88.15
Percentage (%)	Small pore	4.73	5.07	5.23	7.27	10.78
	Mesopore	0.51	1.00	0.80	0.53	1.07
	Macropore	0.31	0	0.02	0.01	0
Pore area	Micropore	8.31	15.10	21.90	30.90	30.78
Percentage (%)	Small pore	4.68	12.73	21.53	30.50	45.25
	Mesopore	10.58	72.17	23.27	23.80	23.97
	Macropore	76.43	0	33.30	14.80	0

macropores and mesopores decreases, while the area of small pores and micropores increases, especially for small pores.

Table 2 illustrates the number and area percentage of these four types of pores in specimens from each soil layer. The number and area percentage of the four types of pores present a similar distribution in all five specimens. The number of micropores, small pores, mesopores and macropores decreased significantly in each specimen. More specifically, the number of micropores in each specimen showed a strong relation to total pore number, and the number percentage of micropores decreased from 94.64% from two meters deep to 88.15% from ten meters deep. However, the contribution of small pores to the total pore number increased from 4.80 to 10.78%. Mesopores and macropores contributed very little to the total pore number.

However, the contribution of micropores to the total pore area increased significantly from 8.31% from 2 m deep to 30.78% from 10 m deep, which shows an opposite trend to its number distribution. The area of small pores also increased, from 4.68 to 45.25%. Additionally, the areas of meso- and macropores were responsible for approximately 87% of the total pore area in sample from 2 m deep, but this contribution of meso- and macropores decreased to 24% in the sample from 10 m deep. Thus, approximately 62% area reduction for macro- and mesopores, 22% area increase for small pores and 40% area increase for micropores were resulting from overburden pressure.

Pore shape distribution in different types of pores

Pore shape factor (*F*) was used in this work to determine the pore shape distribution in the five samples.

$$F = \frac{A_{\text{Pore}}}{P_{\text{pore}}^2} \tag{2}$$

where A_{pore} is the area of each single pore and P_{pore} is the perimeter of each single pore. The *F* values were <0.015 for elongated pores, from 0.015 to 0.04 for irregular pores, and >0.04 for rounded pores. The distributions of these

three different pore shapes in micropores, small pores, mesopores and macropores for sample of each soil layer are presented in Fig. 8.

The distribution of pore shapes in micropores, small pores, mesopores and macropores exhibited a similar pattern in the five specimens (Fig. 8). Specifically, micropores were dominated by rounded pores (80%), with the remaining 20% dominated by irregular pores and a smaller proportion of elongated pores. Small pores consisted of 50% irregular pores, 20% elongated pores and 30% rounded pores. Medium porosity consisted of elongated and irregular pores and macropores were entirely elongated pores. So, the most significant changes in the number of micropores, small pores, mesopores and macropores in Table 2 were mainly due to the differences in the number of round pores, as round pores tend to be small.

In terms of pore shape, the areas of micropores, small pores, mesopores and macropores were dominated by elongated pores, followed by irregular pores and a small area of round pores (Fig. 8). Additionally, the areas of elongated or irregular meso- and macropores showed a significant decrease in the five specimens, while the areas of elongated, irregular and rounded micropores presented an increasing trend in the five specimens. A slight increase can also be found in small pores. Apparently, the 62% area reduction in macro- and mesopores in Table 2 resulted from the overburden pressure, as indicated by the change in elongated and irregular meso- and macropores.

Pore morphology distribution

Figure 9 exhibits the overall morphologic characteristics of all the pores in the five different loess layers, including circularity, convexity, and elongation (Klaver et al. 2015). All parameters vary from 0 to 1, and the three parameters were calculated via the following formulas.

$$\text{Circularity} = \frac{4\pi A_{\text{pore}}}{P_{\text{pore}}^2} \tag{3}$$

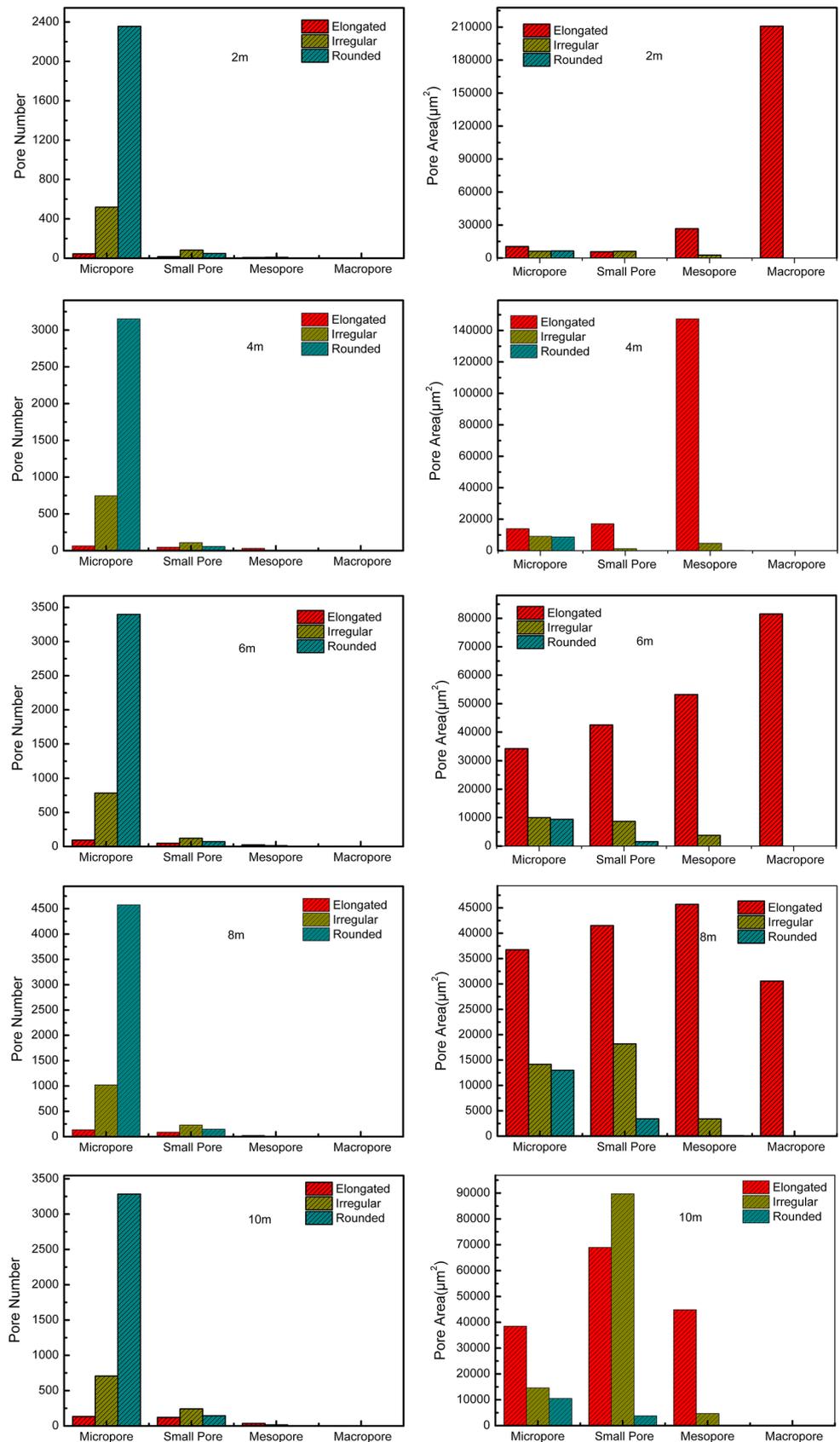
$$\text{Convexity} = \frac{A_{\text{pore}}}{A_{\text{convex hull}}} \tag{4}$$

$$\text{Elongation} = 1 - \left(\frac{W_{\text{pore}}}{L_{\text{pore}}} \right) \tag{5}$$

where $A_{\text{convex hull}}$ is the convex hull of each individual pore, W_{pore} is the short axis of each individual pore, and L_{pore} is the long axis of each individual pore.

The frequency distribution histograms show that the circularity of pores in each specimen exhibited a stationary distribution between 0 and 0.95 and a frequency peak between 0.95 and 1 (Fig. 9). This pattern can also be seen from the slope of the cumulative frequency curve, which indicates that round pores were in the majority. The mean

Fig. 8 Number and area of pores' shapes for different types of pores in the five samples



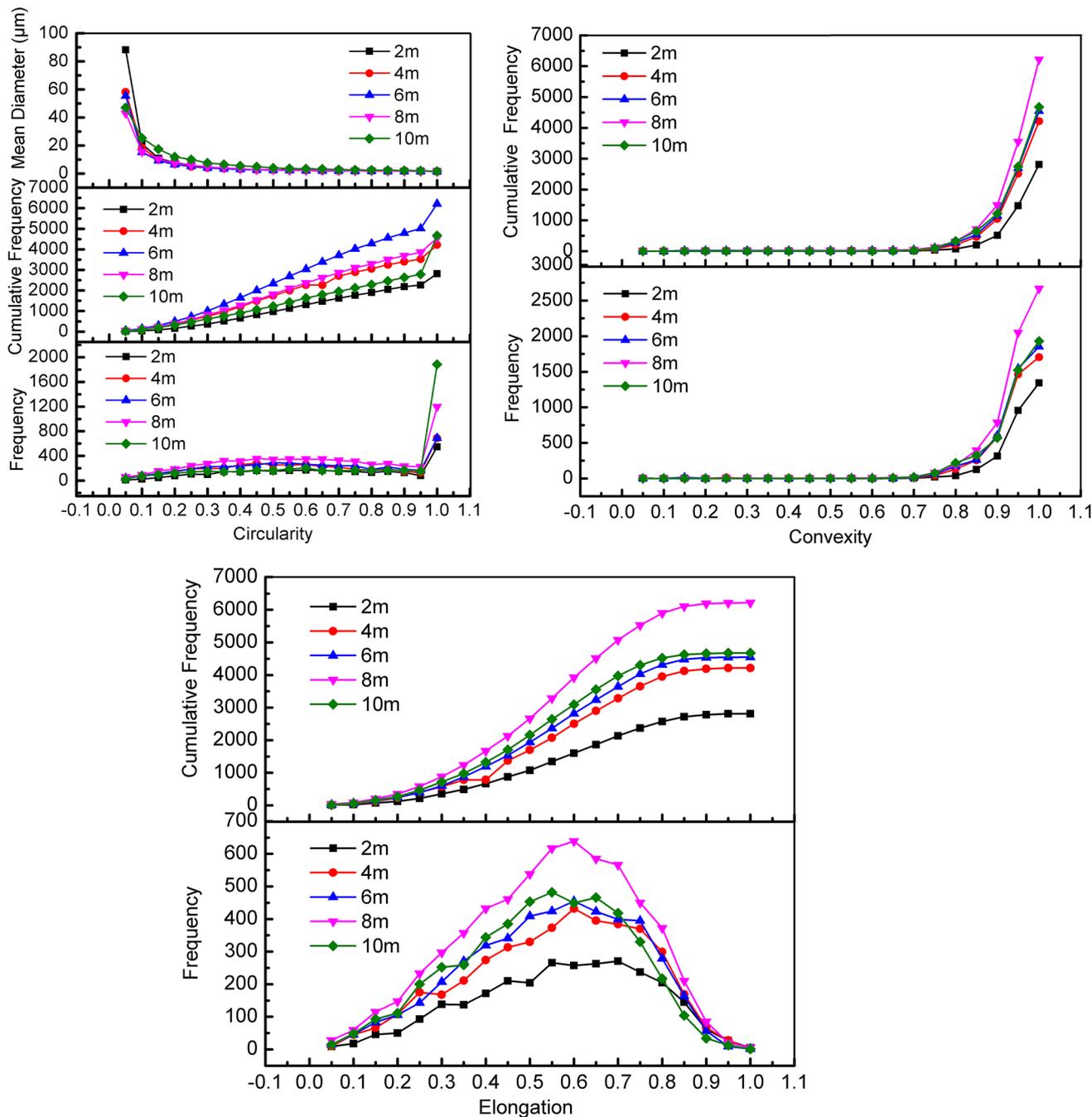


Fig. 9 Pore morphology

diameter of pores decreased with increasing circularity, indicating that the rounder the pore, the smaller the diameter. The cumulative frequency curve of convexity suggests an exponential function distribution, with a frequency stationary between 0 and 0.7, accounting for just 5% of the pore number. Additionally, a rapid growth from 0.7 to 1 was observed, accounting for more than 95% of the total pores. The cumulative frequency curve of elongation formed an S-shaped curve, and its frequency obeyed the

Gaussian distribution or normal distribution with a peak at approximately 0.6. Notably, the pore surfaces in Malan loess tended to be smooth, and most pores were elongated.

Pore structure of loess and its significance in environmental research

The special microstructures of loess, as a typical porous media, make it as an excellent migration channel or storage

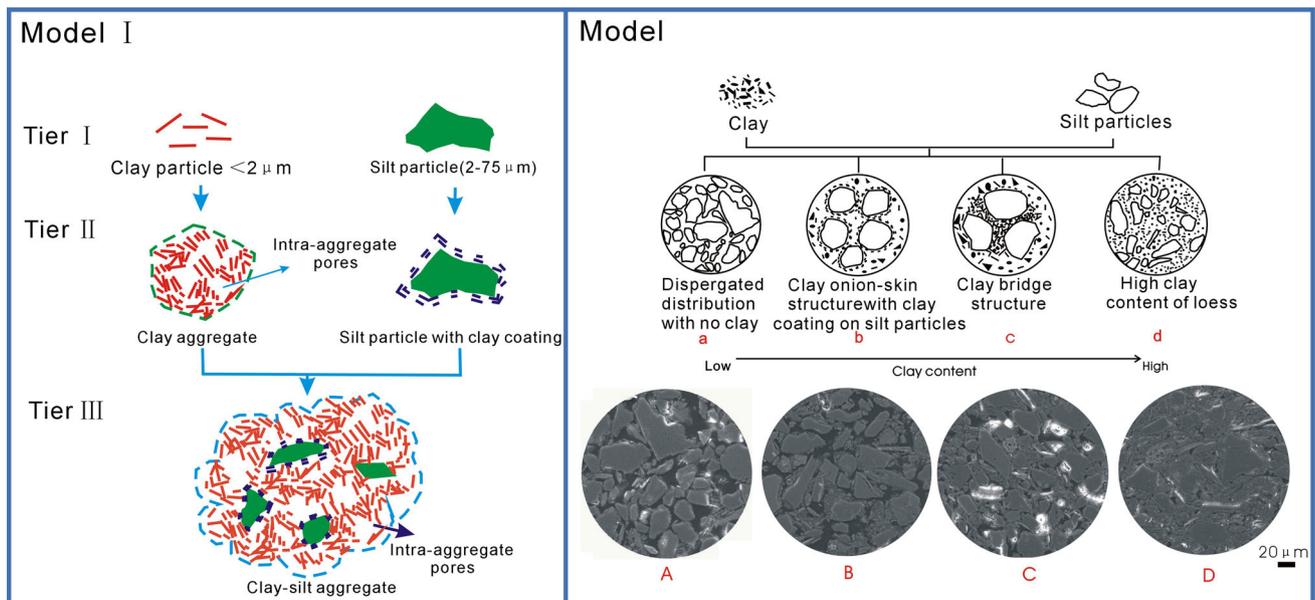


Fig. 10 Conceptual models of loess microstructure at different depths and their corresponding SEM images (“A”, “B”, “C” and “D” are the corresponding SEM images to “a”, “b”, “c” and “d”, respectively)

space for water or contaminants. The porosity, permeability and storage or adsorption capacity of loess are closely related to its microstructures.

First, the characteristics of the pore structure of loess determine the permeability and storage capacity, which consequently influences the transfer characteristics of water and contaminants. Generally, the higher loess porosities, larger average pore diameters and more elongated or irregular large connected pores are associated with better permeability and faster water/contaminant migration rates. Second, the characteristics of the loess particles determine the adsorption capacity of the loess. Generally, finer loess particles or higher proportions of clay particles are associated with larger loess surface areas, resulting in stronger adsorption capacities with respect to contaminants.

In Model I (Fig. 10) from the literature (Liu et al. 2016), clay-silt aggregate is composed of clay and silt particles. Model II (Fig. 10) shows four different types of loess microstructures “a”, “b”, “c” and “d”, as studied in this paper. In Model II a (Fig. 10), loess is composed only of silt particles and lacks clay. Pores formed by a scattered distribution of loess particles mainly belong to macro- or mesopores as classified by diameter, and most are elongated or irregular in shape (Fig. 8). These pores provide spaces for water or contaminants and have a significant relationship with the permeability coefficient and migration rate of water or contaminants in the loess. A 62% areal reduction in macro- or mesopores from the top to bottom layer was found in the loess as demonstrated in Table 2, causing a decreased trend in the permeability and storage capacity of loess with depth. However, the surface area of

loess with this structure (Fig. 10 Model II a) is the smallest among the four types of structures. Thus, this type of loess has the slowest adsorption rate for pollutants. For granule-floor cemented structure (Fig. 10 Model II d), coarse particles are dispersed in a matrix of clayey cemented materials. Due to the dominance of clay and small particle sizes, the surface area of this material is the largest among the four structure types; therefore, the contaminant adsorption capacity is the strongest, and the contaminant migration velocity is the slowest. For clay onion-skin bond structures, clay forms in place via authigenesis, creating a parallel onion-skin-like layer around quartz particles as illustrated in Model II b (Fig. 10). For flocculated clay buttress bonds, the clay forms a random flocculated structure as illustrated in Model II c (Fig. 10), creating a buttress-like structure between bulky grains. The clay contents of “b” and “c” are less than that of “d”, but more than “a”. Therefore, the adsorption rates and migration velocities of contaminants in these two types of loess are intermediate.

Due to the influence of the loess microstructure on permeability, storage and absorption capacity, changing the structure of the loess, e.g., via compression, is a feasible way to protect the loess from pollution, deterioration and/or erosion.

Conclusions

This investigation was conducted to evaluate the pore microstructures in Malan loess at various depths. Macroscopic and image analyses were employed to quantify pore

microstructures in the loess. The results show the following:

1. The variation in the PAR determined via image analysis was in good agreement with the change in porosity obtained from phase relationships for each loess layer. Furthermore, the Malan loess can be characterized as a loose soil according to either the PAR or the porosity. This finding supports the assumption that pores obtained from segmented SEM images were representative of the pore distribution in loess.
2. The number of pores decreased significantly with increasing pore size from micropores to small pores to mesopores to macropores, due to the considerable decrease in the abundance of round pores, indicating that the diameter of round pores tends to be small.
3. The overburden pressure can cause the deformation and breakage of larger pores in loess. Because of increase in the overburden pressure with increasing depth, a 62% areal reduction in macro- and meso-elongated or irregular pores, a 22% increased area of micropores as well as 40% area increase in small pores has been found with the increase in depth.
4. Micropores are dominated by rounded pores (80%). More than 50% of small pores were irregular in shape. Medium pores were elongated and irregular in shape, and macropores were all elongated in shape. The areas of micropores, small pores, mesopores, and macropores were dominated by elongated pores, followed by irregular pores, then by round pores.
5. Elongated and irregular macro- and mesopores contributed significantly on the permeability and water/pollutant migration rate in the loess. Additionally, higher clay contents in the loess were associated with better adsorption capacities.

Acknowledgements The study was supported by the National Natural Science Foundation of China (Grant Nos. 41172255, 41572264, 41440044).

References

Aono Y, Matsushita F, Shibata S, Hama Y (2007) Nano-structural changes of C–S–H in hardened cement paste during drying at 50 °C. *J Adv Concr Technol* 5(3):313–323. doi:10.3151/jact.5.313

Bernardes EE, Mantilla Carrasco EVM, Vasconcelos WL, De Magalhães AG (2015) X-ray microtomography (μ-CT) to analyze the pore structure of a Portland cement composite based on the selection of different regions of interest. *Constr Build Mater* 95:703–709. doi:10.1016/j.conbuildmat.2015.07.128

Bottinelli N, Zhou H, Boivin P, Zhang ZB, Jouquet P, Hartmann C, Peng X (2016) Macropores generated during shrinkage in two paddy soils using X-ray micro-computed tomography. *Geoderma* 265:78–86. doi:10.1016/j.geoderma.2015.11.011

Cetin H (2004) Soil-particle and pore orientations during consolidation of cohesive soils. *Eng Geol* 73(1–2):1–11. doi:10.1016/j.enggeo.2003.11.006

Delage P (2010) A microstructure approach to the sensitivity and compressibility of some Eastern Canada sensitive clays. *Geotechnique* 60(5):353–368. doi:10.1680/geot.2010.60.5.353

Delage P, Marcial D, Cui YJ, Ruiz X (2006) Ageing effects in a compacted bentonite: a microstructure approach. *Geotechnique* 56(5):291–304. doi:10.1680/geot.2006.56.5.291

Fener M, Yesiller N (2013) Vertical pore structure profile of a compacted clayey soil. *Eng Geol* 166:204–215. doi:10.1016/j.enggeo.2013.08.001

Gutierrez NHM, de Nóbrega MT, Vilar OM (2009) Influence of the microstructure in the collapse of a residual clayey tropical soil. *Bull Eng Geol Environ* 68(1):107–116. doi:10.1007/s10064-008-0180-z

Klaver J, Desbois G, Littke R, Urai JL (2015) BIB–SEM characterization of pore space morphology and distribution in post mature to over mature samples from the Haynesville and Bossier Shales. *Mar Pet Geol* 59:451–466. doi:10.1016/j.marpetgeo.2014.09.020

Levitz P (2007) Toolbox for 3D imaging and modeling of porous media: relationship with transport properties. *Cem Concr Res* 37(3):351–359. doi:10.1016/j.cemconres.2006.08.004

Li PY, Qian H, Wu JH (2014a) Accelerate research on land creation. *Nature* 510(7503):29–31. doi:10.1038/510029a

Li P, Wu J, Qian H, Lyu X, Liu H (2014b) Origin and assessment of groundwater pollution and associated health risk: a case study in an industrial park, northwest China. *Environ Geochem Health* 36(4):693–712. doi:10.1007/s10653-013-9590-3

Li PY, Qian H, Wu JH, Chen J, Zhang YQ, Zhang HB (2014c) Occurrence and hydrogeochemistry of fluoride in shallow alluvial aquifer of Weihe River, China. *Environ Earth Sci* 71(7):3133–3145. doi:10.1007/s12665-013-2691-6

Li PY, Wu JH, Qian H (2014d) Hydrogeochemistry and quality assessment of shallow groundwater in the southern part of the Yellow River Alluvial Plain (Zhongwei Section), China. *Earth Sci Res J* 18(1):27–38. doi:10.15446/esrj.v18n1.34048

Li P, Qian H, Howard KWF, Wu J, Lyu X (2014e) Anthropogenic pollution and variability of manganese in alluvial sediments of the Yellow River, Ningxia, northwest China. *Environ Monit Assess* 186(3):1385–1398. doi:10.1007/s10661-013-3461-3

Li PY, Wu JH, Qian H (2016a) Hydrochemical appraisal of groundwater quality for drinking and irrigation purposes and the major influencing factors: a case study in and around Hua County, China. *Arab J Geosci* 9(1):15. doi:10.1007/s12517-015-2059-1

Li PY, Wu JH, Qian H, Zhang YT, Yang N, Jing LJ, Yu PY (2016b) Hydrogeochemical characterization of groundwater in and around a wastewater irrigated forest in the southeastern edge of the Tengger Desert, Northwest China. *Expo Health* 8(3):331–348. doi:10.1007/s12403-016-0193-y

Li P, Zhang Y, Yang N, Jing L, Yu P (2016c) Major ion chemistry and quality assessment of groundwater in and around a mountainous tourist town of China. *Expo Health* 8(2):239–252. doi:10.1007/s12403-016-0198-6

Li PY, Li XY, Meng XY, Li MN, Zhang YT (2016d) Appraising groundwater quality and health risks from contamination in a semiarid region of northwest China. *Expo Health* 8(3):361–379. doi:10.1007/s12403-016-0205-y

Li P, Tian R, Xue C, Wu J (2017) Progress, opportunities and key fields for groundwater quality research under the impacts of human activities in China with a special focus on western China. *Environ Sci Pollut Res* 24(15):13224–13234. doi:10.1007/s11356-017-8753-7

Liu Z, Liu FY, Ma FL, Wang M, Bai XH, Zheng YL, Yin H, Zhang GP (2016) Collapsibility, composition, and microstructure of

- loess in China. *Can Geotech J* 53(4):673–686. doi:[10.1139/cgj-2015-0285](https://doi.org/10.1139/cgj-2015-0285)
- Messing I, Jarvis NJ (1990) Seasonal variation in field-saturated hydraulic conductivity in two swelling clay soils in Sweden. *J Soil Sci* 41(2):229–237. doi:[10.1111/j.1365-2389.1990.tb00059.x](https://doi.org/10.1111/j.1365-2389.1990.tb00059.x)
- Munkholm LJ, Heck RJ, Deen B (2012) Soil pore characteristics assessed from X-ray micro-CT derived images and correlations to soil friability. *Geoderma* 181–182:22–29. doi:[10.1016/j.geoderma.2012.02.024](https://doi.org/10.1016/j.geoderma.2012.02.024)
- Muñoz-Castelblanco JA, Pereira JM, Delage P, Cui YJ (2012) The water retention properties of a natural unsaturated loess from northern France. *Geotechnique* 62(2):95–106. doi:[10.1680/geot.9.P.084](https://doi.org/10.1680/geot.9.P.084)
- Nie BS, Liu XF, Yang LL, Meng JQ, Li XC (2015) Pore structure characterization of different rank coals using gas adsorption and scanning electron microscopy. *Fuel* 158:908–917. doi:[10.1016/j.fuel.2015.06.050](https://doi.org/10.1016/j.fuel.2015.06.050)
- Pagliai M, Vignozzi N, Pellegrini S (2004) Soil structure and the effect of management practices. *Soil Tillage Res* 79(2):131–143. doi:[10.1016/j.still.2004.07.002](https://doi.org/10.1016/j.still.2004.07.002)
- Pires LF, Cooper M, Cássaro FAM, Reichardt K, Bacchi OOS, Dias NMP (2008) Micromorphological analysis to characterize structure modifications of soil samples submitted to wetting and drying cycles. *Catena* 72(2):297–304. doi:[10.1016/j.catena.2007.06.003](https://doi.org/10.1016/j.catena.2007.06.003)
- Promentilla MAB, Sugiyama T, Hitomi T, Takeda N (2009) Quantification of tortuosity in hardened cement pastes using synchrotron-based X-ray computed microtomography. *Cem Concr Res* 39(6):548–557. doi:[10.1016/j.cemconres.2009.03.005](https://doi.org/10.1016/j.cemconres.2009.03.005)
- Rasa K, Horn RF, Rätty M, Yli-Halla M, Pietola L (2009) Shrinkage properties of differently managed clay soils in Finland. *Soil Use Manag* 25(2):175–182. doi:[10.1111/j.1475-2743.2009.00214.x](https://doi.org/10.1111/j.1475-2743.2009.00214.x)
- Rasa K, Eickhorst T, Tippkötter R, Yli-Halla M (2012) Structure and pore system in differently managed clayey surface soil as described by micromorphology and image analysis. *Geoderma* 173–174:10–18. doi:[10.1016/j.geoderma.2011.12.017](https://doi.org/10.1016/j.geoderma.2011.12.017)
- Romero E, Simms PH (2008) Microstructure investigation in unsaturated soils: a review with special attention to contribution of mercury intrusion porosimetry and environmental scanning electron microscopy. *Geotech Geol Eng* 26(6):705–727. doi:[10.1007/s10706-008-9204-5](https://doi.org/10.1007/s10706-008-9204-5)
- Romero E, Gens A, Lloret A (1999) Water permeability, water retention and microstructure of unsaturated compacted Boom clay. *Eng Geol* 54(1–2):117–127. doi:[10.1016/S0013-7952\(99\)00067-8](https://doi.org/10.1016/S0013-7952(99)00067-8)
- Sveistrup TE, Haraldsen TK, Langohr R, Marcelino V, Kværner J (2005) Impact of land use and seasonal freezing on morphological and physical properties of silty Norwegian soils. *Soil Tillage Res* 81(1):39–56. doi:[10.1016/j.still.2004.05.004](https://doi.org/10.1016/j.still.2004.05.004)
- VandenBygaart B, Protz R, Tomlin AD (1999) Changes in pore structure in a no-till chronosequence of silt loam soils, southern Ontario. *Can J Soil Sci* 79(1):149–160. doi:[10.4141/S98-034](https://doi.org/10.4141/S98-034)
- Wan KS, Xu Q (2014) Local porosity distribution of cement paste characterized by X-ray micro-tomography. *Sci China Technol Sci* 57(5):953–961. doi:[10.1007/s11431-014-5513-5](https://doi.org/10.1007/s11431-014-5513-5)
- Wen BP, Yan YJ (2014) Influence of structure on shear characteristics of the unsaturated loess in Lanzhou. *China Eng Geol* 168:46–58. doi:[10.1016/j.enggeo.2013.10.023](https://doi.org/10.1016/j.enggeo.2013.10.023)
- Wu J, Sun Z (2016) Evaluation of shallow groundwater contamination and associated human health risk in an alluvial plain impacted by agricultural and industrial activities, mid-west China. *Expo Health* 8(3):311–329. doi:[10.1007/s12403-015-0170-x](https://doi.org/10.1007/s12403-015-0170-x)
- Yang BH, Wu AX, Miao XX, Liu JJ (2014) 3D characterization and analysis of pore structure of packed ore particle beds based on computed tomography images. *Trans Nonferrous Met Soc China* 24(3):833–838. doi:[10.1016/S1003-6326\(14\)63131-9](https://doi.org/10.1016/S1003-6326(14)63131-9)